Development of quantitative atomic modeling for tungsten transport study using LHD plasma with tungsten pellet injection

I. Murakami[1,2], H. A. Sakaue[1], C. Suzuki[1], D. Kato[1,2], M. Goto[1,2], N. Tamura[1], S. Sudo[1,2], S. Morita[1,2], and LHD Experiment Group[1]

[1]National Institute for Fusion Science, 322-6 Oroshi-cho, Toki, Gifu 509-5292, Japan
[2]SOKENDAI (The Graduate University for Advanced Studies), Hayama, Kanagawa, 240-0193, Japan

E-mail contact of main author: murakami.izumi@nifs.ac.jp

Abstract. Quantitative tungsten study with reliable atomic modeling is important for successful achievement of ITER and fusion reactors. We have developed tungsten atomic modeling for understanding the tungsten behavior in fusion plasmas. The modeling is applied to the analysis of tungsten spectra observed from plasmas of the Large Helical Device (LHD) with tungsten pellet injection. We found that extreme ultraviolet (EUV) emission of W^{24+} to W^{33+} ions at 1.5-3.5nm are sensitive to electron temperature and useful to examine the tungsten behavior in edge plasmas. We can reproduce measured EUV spectra at 1.5-3.5nm by calculated spectra with the tungsten atomic model and obtain charge state distributions of tungsten ions in LHD plasmas at different temperature around 1keV. Our model is applied to calculate the unresolved transition array (UTA) seen at 4.5-7nm tungsten spectra. We analyze the effect of configuration interaction on population kinetics related to the UTA structure in detail and find importance of two-electron-one-photon transitions between $4p^5 4d^{n+1}$ – $4p^6 4d^{n-1} 4f$. Radiation power rate of tungsten due to line emissions is also estimated with the model and is consistent with other models within factor 2.

Keywords: tungsten atomic model, EUV spectra, impurity behavior

1. Introduction

Tungsten is planned to be used as plasma-facing material of the divertor target for ITER and future fusion reactors, because of high melting point, low sputtering yield by hydrogen, and low tritium

inventory. ASDEX Upgrade replaced the first wall and divertor plates as tungsten and JET installed ITER-like wall and tungsten divertor [1,2] and it is reported that tungsten is sputtered due to light impurities such as carbon, boron, and beryllium. Sputtered tungsten is transferred into the main plasma and causes radiation power loss to cool plasma. Tungsten is not fully ionized even in the core of ITER plasma with an electron temperature of 15–30 keV, where tungsten is ionized up to W^{71+} (Li-like tungsten), and radiation power of such tungsten ions is large. It is important for the stable operation of ITER to study the influx and edge transport of tungsten ions. Tungsten behaviour in plasmas can be studied with a spectroscopic method, and we need a reliable atomic model for tungsten to analyze spectral data to obtain reliable information on tungsten in plasmas.

Post et al. [3] provided atomic data sets of ionization and recombination rates and radiation power coefficients for various ions including tungsten and it is called as ADPAK and used widely for plasma simulations. But the atomic data in the ADPAK are based on average ion model and have large uncertainties due to simplified atomic structure especially for N shell or lower charged ions. Asmussen et al. [4] modified ionization rates of tungsten ions in the ADPAK by comparison with spectroscopic measurements in ASDEX Upgrade. These data sets of ionization and recombination rates can be used to calculate charge state distributions of tungsten in ionization equilibrium, but are not for spectroscopic modelling. Pütterich et al. [5] analyzed tungsten emission lines measured in ASDEX Upgrade to obtain ion abundances and estimated correction factors for recombination rates of ADPAK. Ionization rates are taken from the calculation with configuration averaged distorted wave method by Loch et al. [6] in their analysis. They also modelled tungsten spectra to compare with measured spectra for several wavelength regions with tungsten atomic data calculated in the frame work of ADAS [7]; i.e. energy levels, transition probabilities, and electron-impact excitation rate coefficients were obtained with Cowan's atomic code [8]. The excitation rate coefficients are calculated based on Coulomb-Born approximation which is reliable only for high collision energy. Pütterich et al. [9] extended their work to calculate the radiation power rates with two atomic data sets, i.e. one is calculated as configuration averaged energy levels with many electron configurations for each ion and the other is calculated as fine structure energy levels with limited electron

configurations for W^{q+} with $q \geq 26$. Line radiation rate coefficients from two atomic data sets agreed within factor ~2. In JET they used the model to estimate tungsten concentration from soft X-ray imaging and VUV spectroscopy [10].

Tungsten extreme ultraviolet (EUV) spectra measured for plasmas with electron temperature 1-2keV has characteristic feature as a so-called unresolved transition array (UTA) at 4.5-7.0nm [4, 11, 12, 13, 14]. Tungsten UTA has a wide and strong peak at ~5nm and a second wide peak at ~6nm and this structure is thought to be produced by numerous inseparable lines of the principal quantum number n = 4-4 transitions of tungsten N-shell ions. Pütterich et al. [5] tried to reproduce the UTA spectra measured in ASDEX Upgrade with their model described above, but they did not reproduced the second peak at ~6nm. Pütterich et al. [15] performed detailed calculation for atomic data of W^{23+} with FAC code [16] and modeled the spectrum for W^{23+} using 10934 levels, which showed a peak at 5.8nm. Although there were no significant emission peaks in the spectra taken in Berlin electron beam ion trap (EBIT) [17] corresponding to lower charged tungsten ions, they examined the possibility of the contribution from W^{14+} - W^{27+} ions to produce the 6-nm peak and concluded it is not likely to happen in plasmas in ASDEX Upgrade because these ions exist in thin layers at the plasma edge and their contributions are small. They suggested the other possibilities to produce the 6-nm peak with additional processes such as dielectronic recombination in tokamak plasmas and/or with numerous transitions between many electron configurations which were not included in their model.

Foster [18] also calculated tungsten atomic data in the ADAS frame and opened as baseline data sets in OPEN-ADAS [19]. He produced three sets of atomic data; one with configuration averaged energy levels of many electron configurations for each ion (arf40_cl series), one with J-unresolved LS levels (arf40_ls series), and one with J-resolved fine structure energy levels with limited electron configurations (arf40_ic series) because they limited total number of energy levels up to around 2000. All data sets are available for public, but not enough to reproduce the UTA structure.

We have developed a tungsten atomic model with detailed atomic structure including many electron configurations, and we validated the model by comparing with EUV spectra measured from

the CoBIT plasmas [20] with tungsten hexacarbonyl vapour and from the LHD plasmas with tungsten pellet injection. The LHD discharge is entirely stable for substantial amount of tungsten injection exhibiting no MHD instabilities. The CoBIT experiments well control the charge distribution of tungsten ions by changing the electron beam energy which determines the highest charge state in the plasma and by controlling the vapour gas pressure of hexacarbonyl. The information from the CoBIT spectra is absolutely helpful to identify the EUV lines in the LHD.

In this paper we report our tungsten atomic model and application to spectroscopic analysis of LHD plasma to understand properties of tungsten ions in LHD plasma with electron temperature 0.5 – 3keV, which corresponds to peripheral plasma of ITER. In the following sections, our tungsten atomic model is explained in section 2, and the spectroscopic experiments in the CoBIT and the LHD are shown in section 3. We discuss the results of charge state distributions obtained by analyzing EUV spectra of LHD discharge in section 4 and estimate radiation power loss in section 5. Summary is given in section 6.

2. Tungsten atomic model

As the tungsten atomic model, we have constructed a collisional-radiative (CR) model for tungsten ions. We solve rate equations for population densities $n(i)$ of excited levels for each ion with quasi-steady state assumption for given electron temperature and density, because the relaxation timescale of the population densities for excited levels is fast enough compared to the timescales for changes in electron density and temperature. We include electron-impact ionization, excitation and de-excitation processes, and radiative decay in the rate equations. The rate equation for the excited level i is described as

$$\begin{aligned} dn(i)/dt = &\sum_{j<i}\{C(j,i)n_e n(j)\} + \sum_{k>i}\{F(k,i)n_e + A(k,i)\}n(k) \\ &-[S(i)n_e + \sum_{k>i} C(i,k)n_e + \sum_{j<i}\{F(i,j)n_e + A(i,j)\}]n(i), \end{aligned} \tag{1}$$

where $C(j,i)$ and $F(k,i)$ are electron-impact excitation and de-excitation rate coefficients, n_e is electron density, $A(k,i)$ is the radiative transition probability, and $S(i)$ is the electron-impact ionization rate

coefficient. The recombination processes are not included in this model. These contributions could be small for plasmas considered here. Energy levels, radiative transition probabilities, electron-impact excitation, and ionization cross sections are calculated with the HULLAC code (version 9) [21]. In the HULLAC code, atomic structure is calculated with Dirac Hamiltonian using parametric potential method and configuration interaction is included. The radiative transition probabilities for electric dipole and quadrupole and magnetic dipole and quadrupole transitions are calculated. Collision cross sections are calculated with a relativistic distorted wave method, which is reliable over a wide range of collision energy. We consider electron configurations with principal quantum number n up to 6 at least including inner-shell excited states for atomic structure and up to about 23,000 J-resolved fine-structure levels for one ion are included in the CR model. As an example, energy levels of W^{33+} ion are shown in Figure. 1. We consider 24 electron configurations, i.e., $4s^24p^64d^5$, $4s^24p^54d^6$, $4s^24p^64d^4nl$ (n = 5–6 and l = 0–4), $4s^24p^54d^5nl$ (n = 5–6 and l = 0–4) states and 22,647 fine-structure levels in total, whereas ADAS dataset “arf40_ic_w33.dat” for fine structure J-resolved levels includes only 5 configurations [18]. Note 28 configurations are considered for W^{32+} ion to calculate the cooling factor with the configuration averaged energy levels in [9]. Rate coefficients for electron-impact excitation and ionization processes are obtained by averaging with electron velocity distribution as $C(i, j) = \langle \sigma(i,j)\boldsymbol{v} \rangle$. We use the Maxwellian velocity distribution to compare with spectra taken in the LHD, and mono-energy distribution for CoBIT spectra. Here we examine W^{q+} ions with q = 20–45 and they are N-shell ions, i.e., the outermost electron is in n = 4 shell for the ground state. Ionization potentials for these ions are 543–2,414eV [22] and they can be seen in LHD plasmas.

Spectral line intensities are obtained with the population densities of the upper level for the transition as

$$I(i, j; T_e, n_e) = n(i)\, A(i, j)\Delta E(i,j), \qquad (2)$$

where $\Delta E(i,j)$ is the transition energy and $n(i)$ is the population density calculated by the CR model with given electron density n_e and temperature T_e.

Our CR model calculates tungsten spectrum for each ion and we need charge state distribution of tungsten ions to synthesize a spectrum to compare with measured one. As an example, we use charge state distribution calculated by Sasaki and Murakami with ionization equilibrium assumption [23] and synthesize EUV spectra at 2–7 nm as shown in Figure 2. Typical EUV spectrum measured in the LHD is also shown in Figure 2. Similarly to the previous works [5, 11, 12, 13, 14], the first peak of the UTA at ~5 nm is mainly produced with $4p^6 4d^{n-1} 4f$ – $4p^6 4d^n$ (4f-4d transition) and $4p^5 4d^{n+1}$ – $4p^6 4d^n$ (4d-4p transition) transitions of W^{29+}–W^{34+} ions and $4p^6 4d^9 4f^{n+1}$ – $4p^6 4d^{10} 4f^n$ transitions (4f–4d transition) of W^{25+}–W^{28+} ions . Corresponding to the second peak at around 6nm in the LHD spectrum, there are many lines: 4d-4p transitions of $4p^5 4d^{n+1}$ – $4p^6 4d^n$ (W^{29+}–W^{34+} ions) and $4p^5 4d^{10} 4f^{n+1}$ – $4p^6 4d^9 4f^{n+1}$ (W^{23+}–W^{28+} ions) transitions, and 4f-4d transitions of $4p^6 4d^9 4f^{n+1}$ – $4p^6 4d^{10} 4f^n$ and $4p^6 4d^9 4f^n 5l$ – $4p^6 4d^{10} 4f^{n-1} 5l$ transitions (W^{23+}–W^{28+} ions), and 5d-4f transition of $4p^6 4d^{10} 4f^n 5d$ – $4p^6 4d^{10} 4f^{n+1}$ transitions (W^{21+}–W^{23+} ions). Due to the configuration interaction (CI) between $4p^5 4d^{n+1}$ and $4p^6 4d^{n-1}$ 4f configurations of W^{29+}–W^{34+} ions, radiative transition probabilities of many 4f-4d transitions at ~6nm are reduced one order of magnitude or more and 4f-4d transitions at ~5nm are enhanced for some factors, compared to the cases without CI in atomic structure calculations. In addition, two-electron-one-photon transitions from $4p^5 4d^{n+1}$ to $4p^6 4d^{n-1}$ 4f configurations are produced by CI. Our model includes higher inner-shell excited levels, such as $4p^5 4d^n 4f$ and $4p^5 4d^n 5l$ levels, and electron-impact excitation to such higher levels can be followed by cascade or de-excitation processes to $4p^5 4d^{n+1}$ levels, which can enhance population densities of the $4p^5 4d^{n+1}$ level. On the other hand, population flows from $4p^5 4d^{n+1}$ to $4p^5 4d^{n-1}$ 4f levels reduce the population density of $4p^5 4d^{n+1}$ level. Thus 4d-4p transitions at ~6nm with smaller transition probabilities become less prominent and 4f-4d transitions at ~5nm are much more enhanced in spectra with Te=0.53 and 1keV as shown in Fig.2b, compared to the cases without CI. The concentration to 4f-4d transitions at ~4.8nm due to CI is very strong for W^{28+} - W^{34+} ions. Figure 3 demonstrates the change of UTA structure due to CI for W^{33+} ion. Due to CI strong concentration at ~5nm and weaken structure at ~6nm are seen. The $4d^{10} 4f^{n-1} 5d$ – $4d^{10} 4f^n$ transitions of W^{21+}–W^{23+} ions (5d–4f transition) can contribute to the second peak at ~6nm. The wavelength of the 5d-4f transition has strong

dependence on the charge states similarly to the other n=5-4 transitions such as 5g-4f transition (see next section), as suggested in [14]. Only limited charge state can contribute to the UTA. In order to reproduce the 6-nm peak of the UTA, population densities are required to be enhanced for $4p^5 4d^{n+1}$ levels (W^{29+}–W^{34+} ions) and $4p^6 4d^9 4f^{n+1}$ levels (W^{23+}–W^{28+} ions). Cascade processes from higher levels such as dielectronic recombination process and charge exchange process with neutral hydrogen could enhance population densities of these levels. The population outflow from $4p^5\ 4d^{n+1}$ levels is sensitive to the transition probabilities of two-electron-one-photon transitions, $4p^5 4d^{n+1} - 4p^6 4d^{n-1} 4f$, which is strongly dependent on physics of CI. Evaluation on the transition probabilities for these two-electron-one-photon transitions will be required. For the higher electron temperature case (T_e = 2 keV), W^{37+}–W^{47+} ions do not produce UTA and isolated lines appear, as shown as the dotted line in Figure 2b.

3. Spectroscopic measurements in CoBIT and LHD

Tungsten EUV spectra are measured for plasma in the CoBIT [24]. Details of the experimental setup is explained in Ref. [24]. Tungsten hexacarbonyl vapor is introduced into the CoBIT, and tungsten is ionized sequentially by the electron beam and trapped by electrostatic potential well in the axial direction and by electronic space charge potential in the radial direction. EUV spectra at the 1.5–4.5 nm wavelength region were measured with various electron beam energy and the charge states of observed emission peaks are determined. Using the CR model, we calculated EUV spectra with the physical condition of the CoBIT, i.e., $n_e = 10^{16}\ m^{-3}$ and mono-energy electron distribution with the beam energy and identified emission peaks as W^{19+}–W^{33+} ions. When electron beam energy is 0.95keV, emission peaks are identified as 6g-4f and 5g-4f transitions of W^{24+} - W^{28+} ions (Figure 4a) and when electron beam energy is 1.37keV, emission peaks are identified as 5g-4f, 5f-4d, and 5p-4d transitions of W^{28+} - W^{33+} ions (Figure 4d). Spectral property is changed at W^{28+} ion reflecting a change in the atomic structure of tungsten ions. The ground state of W^{28+} ion is $4d^{10}$ and one of W^{27+} ion is $4d^{10}$ 4f. Thus *n*g–4f transitions appear for W^{27+} and lower charged ions with open 4f shell in this

wavelength region, but *nl*–4d transitions appear for W^{28+} and higher charged ions because their ground states do not have 4f electrons. The peak wavelengths shift shorter for higher charge states and they are useful to determine charge state distribution in LHD plasmas.

For LHD plasmas, tungsten is injected as a coaxial impurity pellet (0.1–0.3 mm^{ϕ} x 0.7 mm^{L} tungsten in 0.7 mm^{ϕ} x 0.7 mm^{L} cylindrical carbon) [25] or a tracer-encapsulated solid pellet (TESPEL, 0.5–0.9 mm diameter) [26] in NBI heated discharges. A pellet is ablated in the vicinity of normalized minor radius $\rho \sim 0.8$, and tungsten is ionized and transferred into a core plasma region for discharges with typical central electron density $n_e \sim$ a few $10^{19}\,m^{-3}$. A typical NBI heated discharge with tungsten pellet injection is shown in Figure 5. In this case after a tungsten TESPEL was injected at t = 3.8 s, total radiation power and electron density increased and electron temperature and stored energy decreases. Large increase of total radiation power was caused by tungsten. Electron temperature and stored energy recovered later with continuous NBI heating. Spatial distribution of electron temperature and density of this discharge are shown in Figure 6. Electron temperature at the central region dropped due to large radiation loss by tungsten, reached the minimum temperature ~0.2 keV at t = 4.20 s, and recovered with NBI heating (t = 4.60 and 4.80 s). Electron density increased with keeping nearly flat profile. Flat structure seen at around $\rho = 0.8$ - 0.9 in the electron density profile indicates existence of magnetic island caused by a TESPEL injection. Tungsten was supposed to be accumulated within $\rho < 0.8$.

We measured tungsten EUV spectra using an EUV spectrometer [27] and a SOXMOS spectrometer [28]. Using the EUV spectrometer, we obtained very similar EUV spectra at 1.5–3.5 nm to ones measured in the CoBIT and the spectra changed according to the change of central electron temperature. The spectra for low and high temperature cases are shown in Figures 4b and 4e, measured at t = 4.60 s and t = 4.80 s for the discharge shown in Figure 5, respectively. These spectra are looked quite similar to the CoBIT spectra shown in Figures 4a and 4d, respectively.

In order to reproduce the LHD spectra, we calculated spectra using our CR model with the plastma condition of the LHD, i.e., $n_e \sim 5 \times 10^{19}\,m^{-3}$ and the Maxwellian electron velocity distribution with

given electron temperatures T_e, 0.7 keV (t = 4.60 s) and 1.4 keV (t = 4.80 s) for each ion. We assume single temperature for simplicity, since we assume large part of tungsten ions are accumulated in the central flat temperature area. Figures 7a and 7b show calculated spectra at 1.5 – 4.5nm for each ion, i.e. W^{20+} - W^{28+} ions with T_e = 0.7 keV and W^{28+} - W^{35+} ions with T_e = 1.4 keV, respectively. As predicted by previous works [5, 11, 12], the wavelengths of emission peaks for 5g-4f transition shift shorter for higher charge states of W^{20+} - W^{34+} ions as shown in Figures 7a and 7b. The emission peaks of 5d-4f, and 5f-4d transitions appears in spectra of W^{27+} - W^{34+} ions. We newly predict that the emission peak of 6g-4f transition is significant for W^{20+} - W^{26+} ions (Fig. 7a), and it overlaps with 5f-4d transition at W^{28+} and W^{29+} ions, and becomes weaker and almost disappear for W^{30+} and higher charge ions. For W^{27+} -W^{34+} ions, the 5p-4d transition produces two peaks and wavelength of shorter-wavelength peak of W^{q+} ion nearly accidentally coincides with one of longer-wavelength peak of $W^{(q+1)+}$ ion. Similarly, two peaks of 5f-4d transitions overlap with ones from different charged ion. Thus observed these peaks are blended.

Using these calculated spectra for each ion, we synthesized spectra with ion abundances determined to match with the measured spectra as shown in Figures 4c and 4f. Our model calculations well reproduce the LHD spectra with emission peaks of 6g–4f and 5g–4f transitions of W^{23+} – W^{28+} for electron temperature T_e = 0.7 keV case (Figure 4c), and emission peaks of 5f–4d, 5g–4f, and 5p–4d transitions of W^{28+} – W^{34+} for T_e = 1.4 keV (Figure 4f). This is the first identification of 6g-4f transitions in fusion plasmas.

The determined charge state distributions of tungsten ions are shown in Figure 8. For the lower temperature case, W^{25+} ion is the most abundant (solid circles), and W^{28+} ion is the most abundant for the higher temperature case (solid triangles). Uncertainties are estimated as standard deviation of the χ^2-fitting to the measured spectra. For comparison, we also plot charge distributions in ionization equilibrium calculated by three models [4, 5, 23]. Details are discussed in the next section.

Using obtained charge state distributions, we can synthesize the UTA spectra at 5-7 nm. Figure 9 shows measured UTA spectra using the SOXMOS for the same discharge and synthesized UTA

spectra. Similarly to the spectra shown in Fig.2b, strongly concentrated peak at ~5nm and weak structure at ~6nm are seen. Detailed structure such as UTA peak wavelength and width are different from the measured one. This UTA feature is mainly produced with 4f-4d and 4d-4p transitions, i.e. the n = 4-4 transitions as explained in the previous section. Such $\Delta n = 0$ transitions require quite precise determination of energy levels, but current calculation on atomic structure with the atomic code HULLAC has limitation on the accuracy of energy levels and discrepancies of 0.1-0.2nm in wavelengths are remained for $\Delta n = 0$ transitions. Differences on the UTA width and detailed structures could be caused by incompleteness of the atomic structure in the CR model and by plasma effect of spatial distribution of electron temperature and density along the line-of-sight of measurements. Recombination processes also can change the spectral structure. We do not discuss these differences further in detail here. Improvement on the model will be needed for future study.

4. Charge state distributions

As shown in Figure 8, we obtained charge state distributions of tungsten ions using the EUV spectra at 1.5–3.5nm, and can compare them with expected distributions from ionization equilibrium calculations. Sasaki and Murakami [23] constructed a large-scale collisional-radiative model with configuration averaged levels to calculate tungsten ion densities in ionization equilibrium condition. Many autoionizing levels were included and dielectronic recombination process was treated explicitly as electron-capture to autoionizing levels, followed by radiative decay to bound levels. The excitation-autoionization process is also naturally included in the model. Ionization rate coefficients were calculated with Lotz's empirical formula [29]. Traditionally, ADPAK [3] atomic datasets are widely used for ionization equilibrium calculations. This model is based on an average ion model and detailed atomic structures are not considered. Asmussen et al. [4] proposed to modify the ionization rates of tungsten in this package in order to explain experiments done in ASDEX Upgrade. They increased the ionization rates by a factor of up to 3 for W^{q+} with $q > 30$. A part of this factor is explained as the excitation-autoionization process. We also use their rates to calculate charge state

distributions in ionization equilibrium for a comparison in Fig. 8. The ADAS dataset “scd50_w.dat” and “acd50_w.dat” of collisional-radiative ionization and recombination rate coefficients obtained from the OPEN-ADAS database [15] is also used to calculate the ionization equilibrium distribution. These datasets are based on the work of Pütterich et al. [5]. The original ionization rates are calculated with a configuration averaged distorted wave method by Loch et al. [6]. The original recombination rates are ADPAK and are modified to explain the spectral measurements done in ASDEX Upgrade, as described in Pütterich et al. [5]. Using the CR model calculation with given electron temperature and density, CR ionization and recombination rates are obtained. Note that recently theoretical and experimental studies on dielectronic recombination rate coefficients are carried out for some tungsten ions and strong enhancement of the rate coefficients due to resonances were reported [30-32]. Such larger recombination rates will alter the charge state distribution in ionization equilibrium calculations.

Comparing the calculated equilibrium ion abundance distributions and obtained one from the EUV spectra, the distributions of Sasaki and Murakami model for the same electron temperature are shifted toward higher charge states than the measurements, as shown in Figure 8. To obtain the same maximum charge state in the distributions as to the measurement, lower electron temperature must be assumed, i.e., $T_e \sim 0.4$ keV for the $T_0 = 0.7$ keV case, and $T_e \sim 0.9$ keV for the $T_0 = 1.4$ keV case. On the other hand, the abundance distributions calculated with the modified ADPAK rates of Asmussen et al. [4] show closer maximum charge state to the measurements with almost the same electron temperature for both cases. Interestingly, abundance calculation of ADAS indicates the same tendency, but ADAS results indicate higher temperature and the ones of Asmussen model. The reason that the models of Amussen et al. and the ADAS give the similar charge distribution is probably that they modified atomic data to fit to their experiments. The Sasaki and Murakami model does not modify any atomic data artificially, and their model calculation for the line ratio of W^{44+} and W^{45+} lines shows good agreement with experiments, although their ionization and recombination rates of these ions are both larger than the other models.

The discrepancies between the Sasaki and Murakami model and measurements indicate that ionization of tungsten in their model proceeds to higher charge states than expected from the measurements at a fixed temperature. This hints to either too large ionization rates or too small recombination rates at some lower charge states. As mentioned above, resonances can enhance dielectronic recombination rates as obtained by the recently theoretical and experimental studies [30-32]. Such larger recombination rates could help to make discrepancies smaller.

The EUV spectra at 1.5–3.5 nm of this discharge shown in Figure 4 were measured with 5 ms exposure and show rapid time variation, which seem to follow the change of the central electron temperature. It suggests that the charge state distribution follows the change of electron temperature very well and the tungsten ions could be nearly in ionization equilibrium. We do not include the effects of transport and spatial profiles in this analysis yet, however, Asmussen and other studies [4, 33] suggested that the transport effect to the charge state distributions is very small. Spatial-profile and other effects should be examined to explain the discrepancy of the ion abundance distributions between the measurements and the Sasaki-and-Murakami model. Our atomic model still has some limitation, that is, (i) resonances are not included for the calculation of electron-impact excitation cross sections, which would enhance excitation rate coefficients at lower temperature region; (ii) metastable states are not treated separately in the CR calculations are calculated, which would change the population density distributions for excited states; (iii) electron-impact double ionization process is not considered, which would affect the charge state distribution and the population density distribution; and (iv) recombination processes are not included in the CR calculation, which could enhance the population densities with cascade process. We do not consider E3 octopole transitions for the atomic data in this study, but maybe the effect of E3 transitions is not large for fusion plasmas. In addition, we need independent validation for ionization and recombination rates of tungsten ions by experiments.

5. Radiation power loss

The CR model can provide radiation power coefficients due to line emissions for each tungsten ion. Generally radiation power rate due to tungsten ions is given by

$$L(T_e, n_e) = \sum_z L_z(T_e, n_e) N_z(T_e, n_e) / N_W \quad , \qquad (3)$$

where $L_z(T_e, n_e)$ is the radiation power coefficients of z-th charged ion, $N_z(T_e, n_e)$ is number density of z-th charged ion, and N_W is total tungsten number density. Since the $L_z(T_e, n_e)$ due to line emissions is calculated with the CR model and the ion abundance distributions are obtained from the EUV spectra, we can estimate the radiation power rate of tungsten as shown in Figure 10. Their uncertainties are estimated from the uncertainties of ion abundances determined by the χ^2-fitting to spectra. Intrinsic uncertainties due to the atomic model are difficult to estimate and not included. For comparison, the rates calculated by original ADPAK [3], Pütterich et al. [9], and Sasaki and Murakami [23] are also drawn. These three models show different electron temperature dependence and the peak temperature is distributed around 0.7 – 1.5keV, since their equilibrium charge state distributions are different. Our estimated rates are close to the ones of Pütterich et al., but all are consistent within factor 2. Since we do not include the contribution of recombination and bremsstrahlung to the radiation power rate, our estimated rates should be underestimated. Pütterich et al. [9] obtained the contribution of bremsstrahlung and radiative recombination processes to the total power rate as about 10-30% depending on electron temperature. Sudo et al. [34] also estimated the radiation power loss of tungsten from LHD experiments with different method. They used bolometer radiation power measured just after injected TESPEL was ablated. Their estimated values for tungsten radiation power loss rates are around (1-3)x 10^{-31} Wm^3 at T_e = 1.1-1.5 keV, which are smaller than our estimated values as shown in Fig. 10.

Total radiation power loss due to tungsten in core plasma assumed axial symmetry distribution is given by

$$P = \int L(T_e, n_e) n_e(r) n_z(r) dV \quad , \qquad (4)$$

where integration is performed for whole core plasma with electron and tungsten density

distributions. We know total number of tungsten atoms injected to the plasma as a TESPEL for this discharge as 0.895 10^{18} particles. If we assume nearly constant electron density (5 10^{19} m^{-3}) and temperature (0.7 and 1.4 keV) and 60% of injected tungsten is accumulated in the core and contribute to the radiation power, the total radiation power due to tungsten line emissions could be estimated roughly as P_{rad}(0.7keV) ~ 8.4 (*f*/0.6) MW and P_{rad}(1.4keV) ~ 10 (*f*/0.6) MW, where *f* is a fraction of tungsten atoms in the emitting region. This is quite a rough estimate of the radiation power loss due to tungsten, however, these values are comparable to the total NBI heating power.

6. Summary

We have constructed the tungsten atomic model including many fine structure levels and can use the model for detailed analysis of spectra to examine tungsten behavior in fusion plasmas. The atomic model is validated by comparing calculated spectra with measured ones with the CoBIT and the LHD. We obtained good agreement for EUV spectra of W^{20+} – W^{33+} ions at 1.5–3.5 nm wavelength region for the CoBIT measurements and the model calculation and we identified emission peaks as n = 6–4 and 5–4 transitions. We injected a tungsten pellet into NBI heated discharge of the LHD and obtained tungsten EUV spectra similar to ones measured in the CoBIT. Using emission peaks at 1.5–3.5 nm of n = 5– 4 transitions which are sensitive to electron temperature, we can determine charge state distribution for W^{20+} – W^{33+} ions for the LHD plasma. These ions are produced in plasma with electron temperature from ~ 0.3 keV to ~ 1.5 keV. This temperature region corresponds to peripheral plasma in the ITER. The obtained charge state distributions from EUV spectra are compared with calculations by the atomic model of Sasaki and Murakami [23], modified ADPAK of Asmussen et al. [4], and ADAS in ionization equilibrium. The modified ADPAK and ADAS show similar abundance distribution with the similar electron temperature to the obtained one. But, the theoretical model of Sasaki and Murakami shows discrepancy from the measurements and we need independent validation on ionization and recombination rates. We also estimate the radiation power rates of tungsten ions

using the CR model calculations and obtained charge state distribution, and the rates are consistent with previous works within factor 2. Total radiation power loss is also estimated.

We tried to reproduce the two-peak characteristics of the UTA at 4–7 nm. The second peak at ~ 6 nm could be produced with $4d^9 4f^{n+1}$–$4d^{10} 4f^n$ transition of W^{25+} – W^{28+} ion and $4p^5 4d^{n+1}$–$4p^6 4d^n$ transition of W^{29+} –W^{34+} ions, but reduced population densities and smaller transition probabilities due to the configuration interaction make these emission lines weak and the spectral structure at ~6nm is weak. We need to improve the tungsten modelling including recombination processes for future study.

Acknowledgements

The authors acknowledge all members of the LHD Experiment Group for their technical support and fruitful discussions. IM acknowledges Dr. Michael Busquet for his help to improve Hullac atomic code. This work is supported partly by JSPS Grant-in-Aid for Scientific Research (A) 23246165 and (B) 23340183, JSPS Grant-in-Aid for Young Scientists (B) 23740412, and the JSPS-NRF-NSFC A3 Foresight Program in the field of Plasma Physics (NSFC: No. 11261140328).

References

[1] Neu R.*et al.* 2007 *Plasma Phys. Control. Fus.* **49** B59
[2] Matthews G. F. *et al* 2013 *J. Nucl. Mater.* **438** S2
[3] Post D. *et al.* 1977 *At. Data Nucl. Data Tables* **20** 397
[4] Asmussen K. *et al.*1998 *Nucl. Fusion* **38** 967
[5] Pütterich T. *et al.* 2008 *Plasma Phys. Control. Fusion* **50** 085016
[6] Loch S. D. *et al.* 2005 *Phys. Rev. A,* **72** 052716
[7] Summers H. P. 2004, *The ADAS User Manual*, version 2.6 http://www.adas.ac.uk/
[8] Cowan R. D. 1981, *The Theory of Atomic Structure and Spectra* (Berkeley: Univ. of California Press)
[9] Pütterich T. *et al.*2010 *Nucl. Fusion* **50** 025012
[10] Pütterich T. *et al.* 2012 *EFDA-JET-CP(12)06/22*
[11] Hinnov E. and Mattioli M. 1978 *Phys. Lett.* **66A** 109
[12] Finkenthal M. *et al*. 1988 *Phys. Lett. A* **127** 255
[13] Jonauskas V, Kucas S, Karazija R 2007 *J. Phys. B: At. Mol. Opt. Phys.* **40** 2179

[14] Harte C S *et al*. 2010 *J. Phys. B: At. Mol. Opt. Phys.* **43** 205004
[15] Pütterich T. *et al*. 2013 *AIP Conf. Proc.* **1545** 132
[16] Gu M. 2003 *Astrophys. J.* **582** 1241
[17] Radtke R. *et al.* 2001 *Phys. Rev. A* **64** 012720
[18] Foster A., 2008 Ph.D. Thesis, http://www.adas.ac.uk/
[19] OPEN-ADAS, http://open.adas.ac.uk/
[20] Nakamura N. *et al*. 2008 *Rev. Sci. Instrum.* **79** 063104.
[21] Bar-Shalom A. *et al.* 2001 *J. Quant. Spectr. Rad. Transfer* **71** 169-188
[22] Kramida A., Ralchenko Yu., Reader J., and NIST ASD Team 2013 *NIST Atomic Spectra Database* (ver. 5.1), [Online]. Available: http://physics.nist.gov/asd
[23] Sasaki A. and Murakami I. 2013 *J. Phys. B: At. Mol. Opt. Phys.* **46** 175701
[24] Sakaue H. A. *et al*.2012 AIP Conf. Proc. **1438** 91
[25] Katai R., Morita S., Goto M. *et al*. 2007 *Jpn. J. Appl. Phys.* **46** 3667
[26] Sudo S. 1993 *J. Plasma Fusion Res.* **69** 1349
[27] Chowdhuri M. B., Morita S., Goto M. *et al*. 2007 *Rev. Sci. Instrum.* **78** 023501
[28] Schwob J. L. *et al.* 1987 *Rev. Sci. Instrum.* **58** 1601
[29] Lotz W. 1968 *Z. Phys.* **216** 241
[30] Balance C P *et al*. 2010 *J. Phys. B: At. Mol. Opt. Phys.* **43** 205201
[31] Schippers S *et al*. 2011 *Phys. Rev. A* **83** 012711
[32] Li M *et al*. 2014 *Plasma Sci. Technol.* **16** 182
[33] Morita S *et al*., 2013 *AIP Conf. Proc.* **1545** 143
[34] Sudo S. *et al.* 2014 *Plasma Fusion Res.*, **9** 1202147

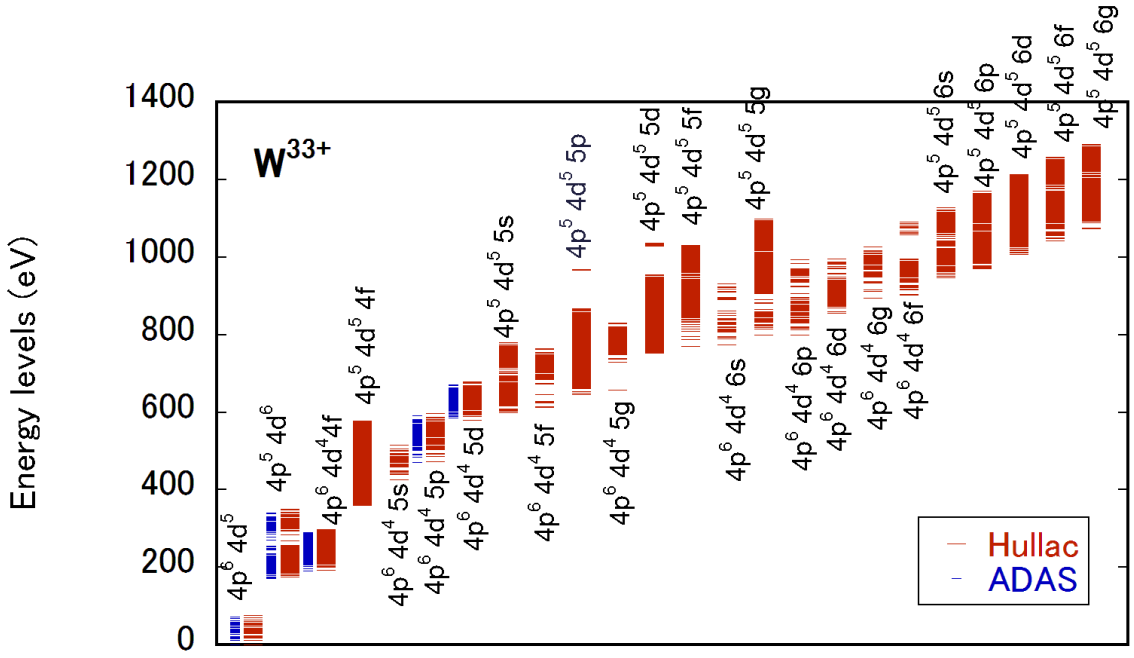

Fig.1 Energy levels for W^{33+} ion, calculated with HULLAC code (red) in our model and data (arf40_ic_w33.dat) in ADAS database (blue) [18,19]. Data in ADAS considers only 5 configurations.

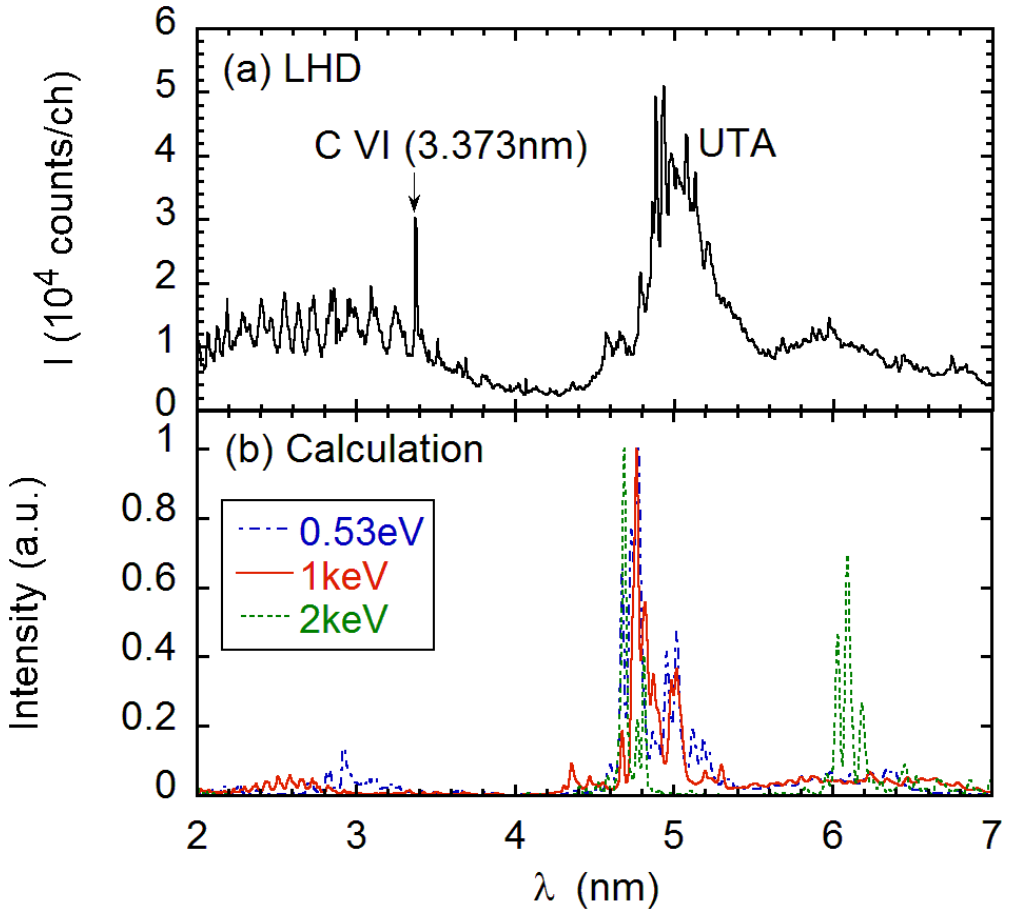

Fig. 2 Tungsten EUV spectra from (a) measurement in LHD and (b) model calculation with assumption of ionization equilibrium with T_e = 0.53 keV (W^{23+} -W^{31+}; dot-dashed line), 1 keV (W^{26+}-W^{36+}; solid line), and 2 keV (W^{37+}-W^{47+}; dotted line). UTA is reproduced at T_e < 1.5 keV and disappears at T_e = 2 keV forming isolated lines.

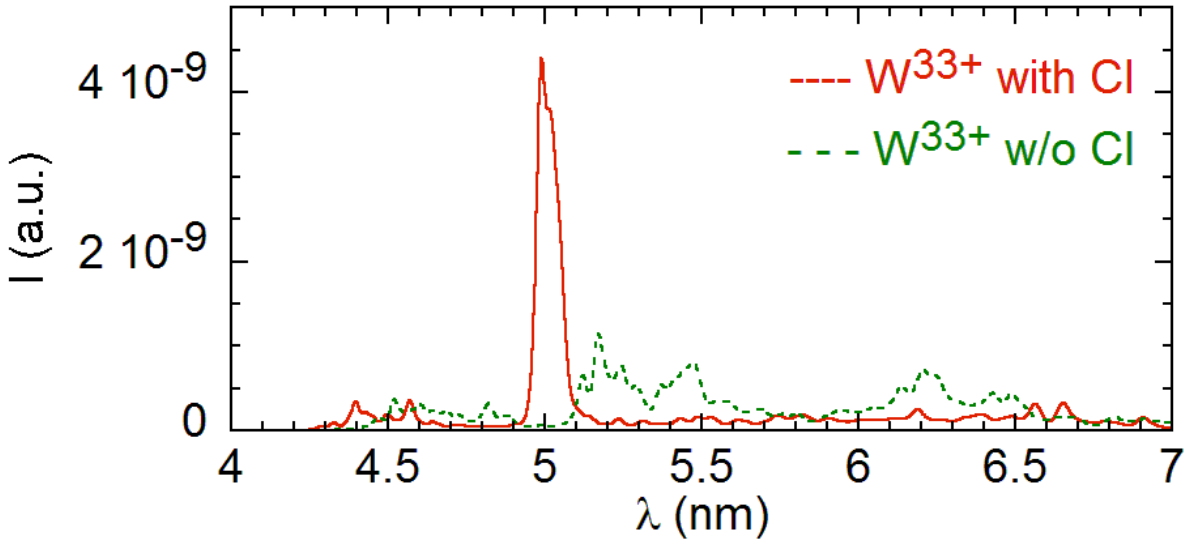

Fig.3 EUV spectra of W^{33+} ion calcualted with atomic data with configuration interaction (CI) (red solid line) and without configuration interaction (green dashed line). Due to the CI, UTA structre changes dramatically.

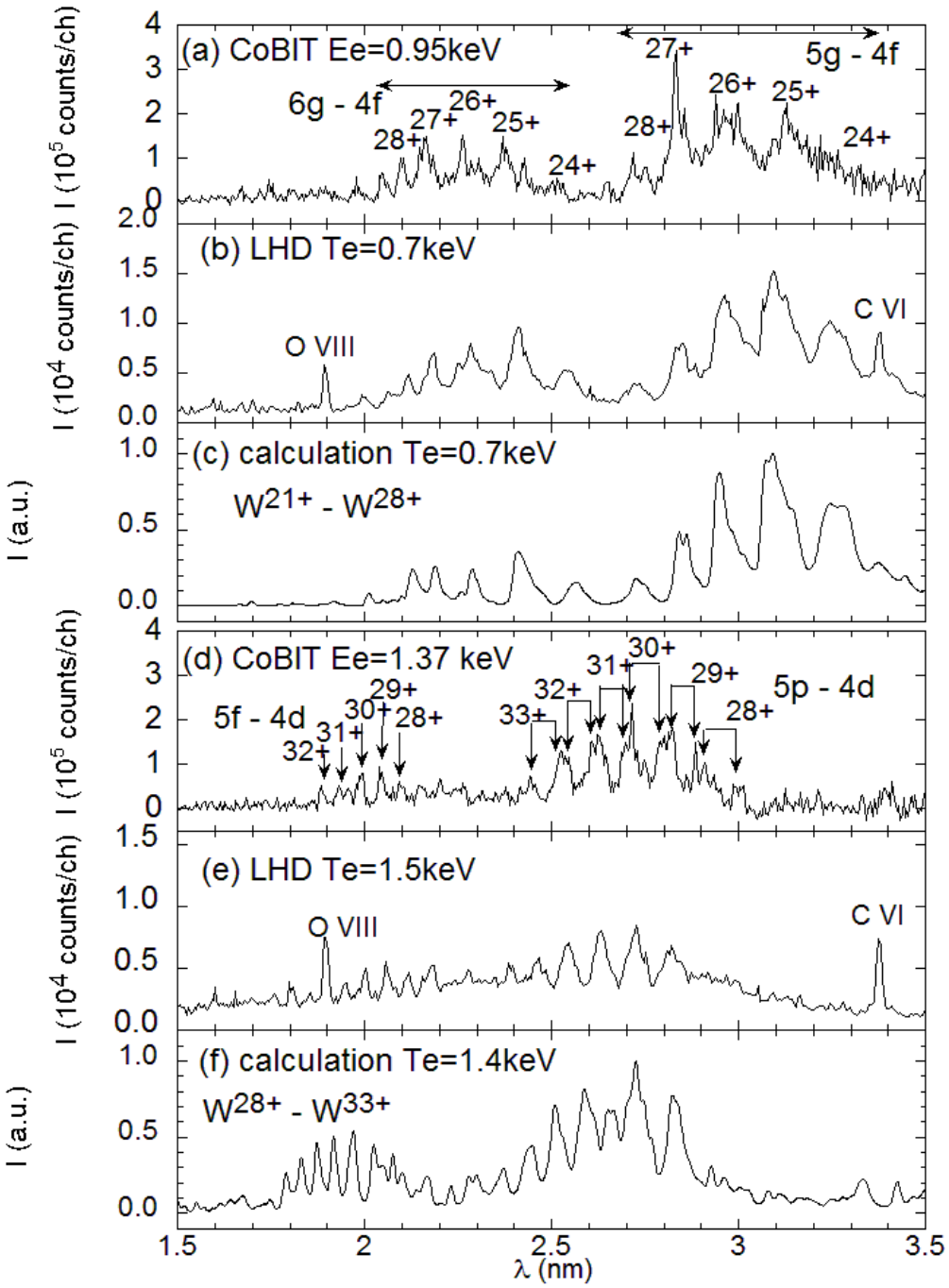

Fig. 4 EUV spectra of tungsten ions; (a, d) CoBIT with two electron beam energies Ee, (b, e) LHD with different central electron temperature T_0 at t= 4.60s and 4.80s of discharge #112880, and model calculations for (c) $W^{21+} – W^{28+}$ and (f) $W^{28+} – W^{33+}$ ions. Wavelengths in calculations at (c) and (f) are shifted by -0.0206nm and 0.0033 nm to fit the position to measurements, respectively.

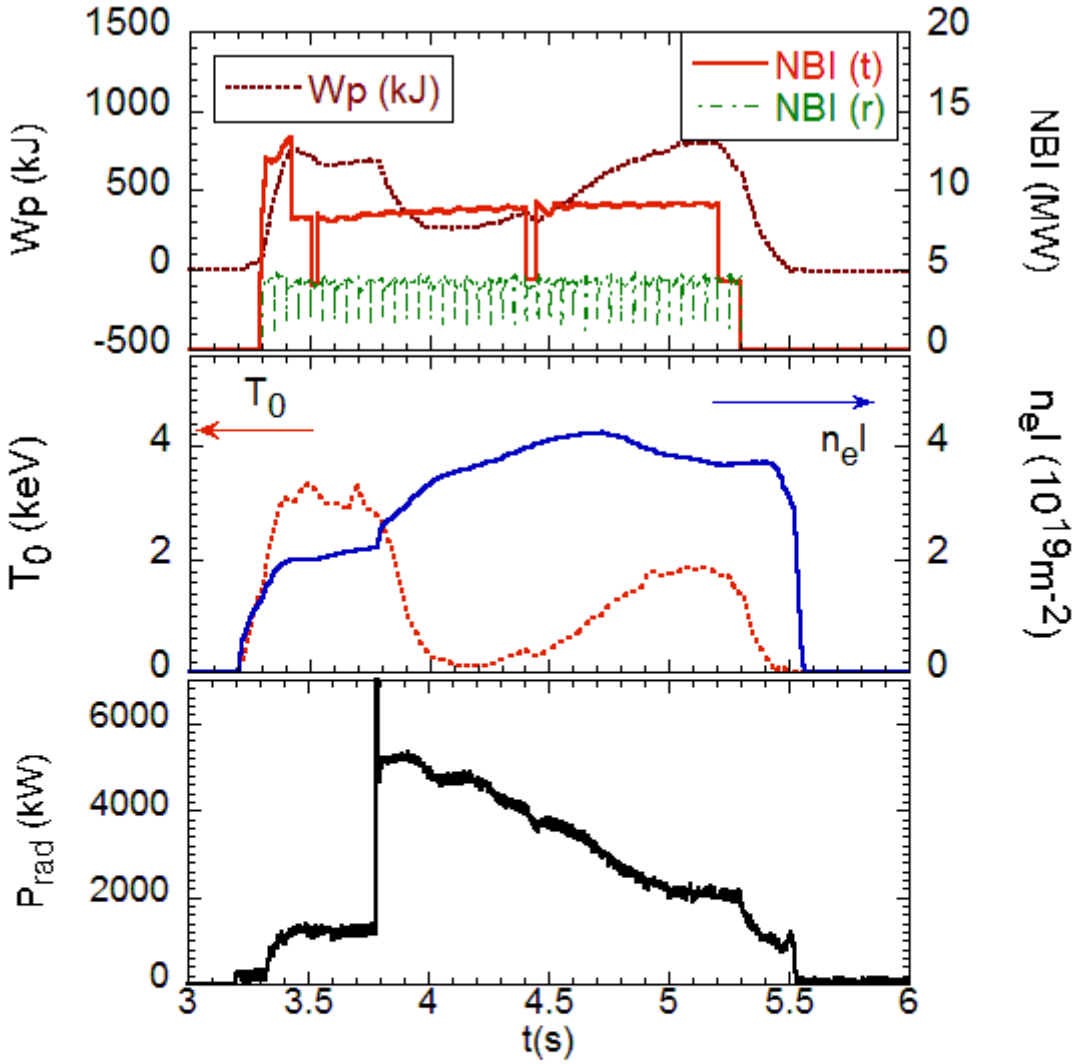

Fig.5 Temporal evolution of stored energy W_p, NBI port-through power, central electron temperature T_0, line-integrated electron density n_el, and total radiation power for discharge #112880 with a tungsten TESPEL injection at 3.8s.

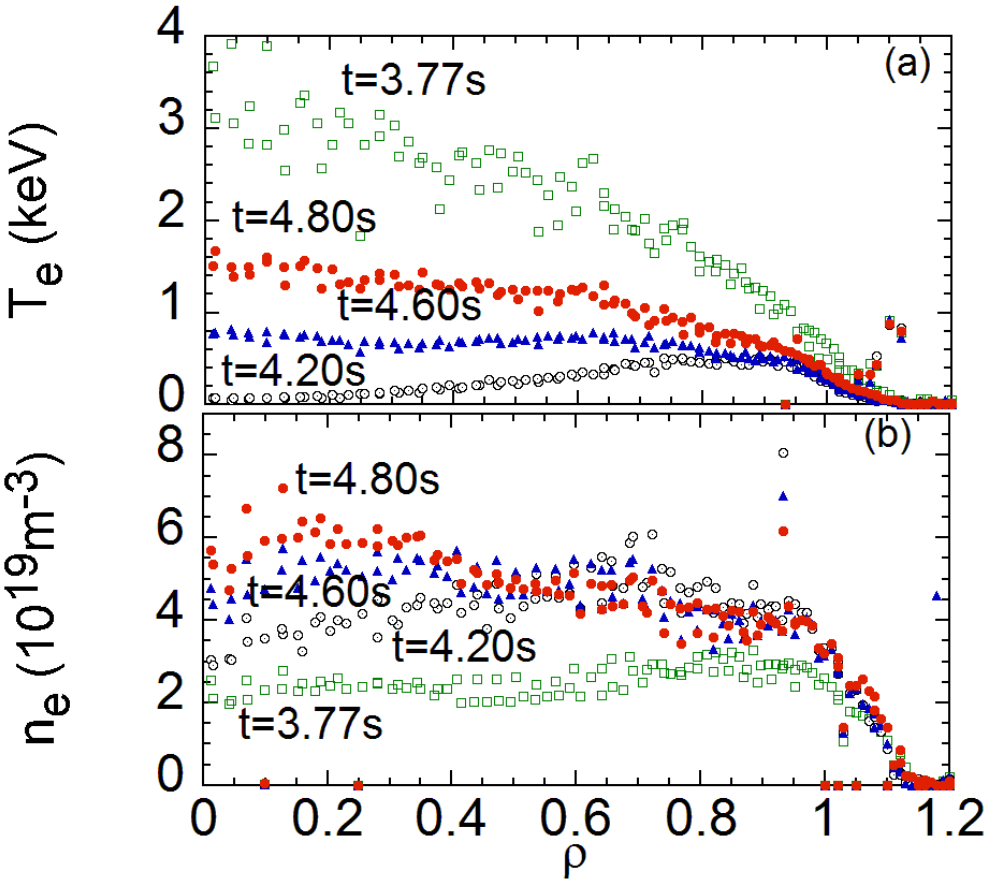

Fig. 6 Electron temperature and density distributions at t=3.77, 4.20, 4.60, and 4.80s for discharge #112880 measured by a Thomson scattering system, as a function of normalized minor radius.

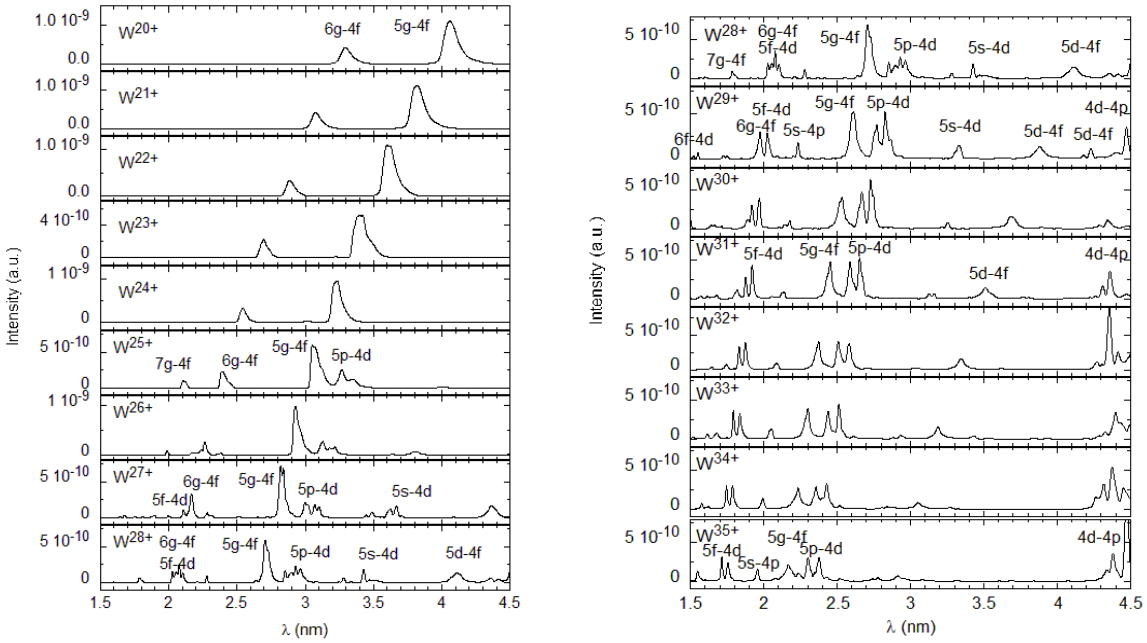

(a) (b)

Figure 7 Calculated spectra for (a) W^{20+} - W^{28+} ions with T_e = 0.7 keV and (b) W^{28+} - W^{35+} ions with Te =1.4keV. Electron density is assumed as 5 $10^{19} m^{-3}$ for both cases.

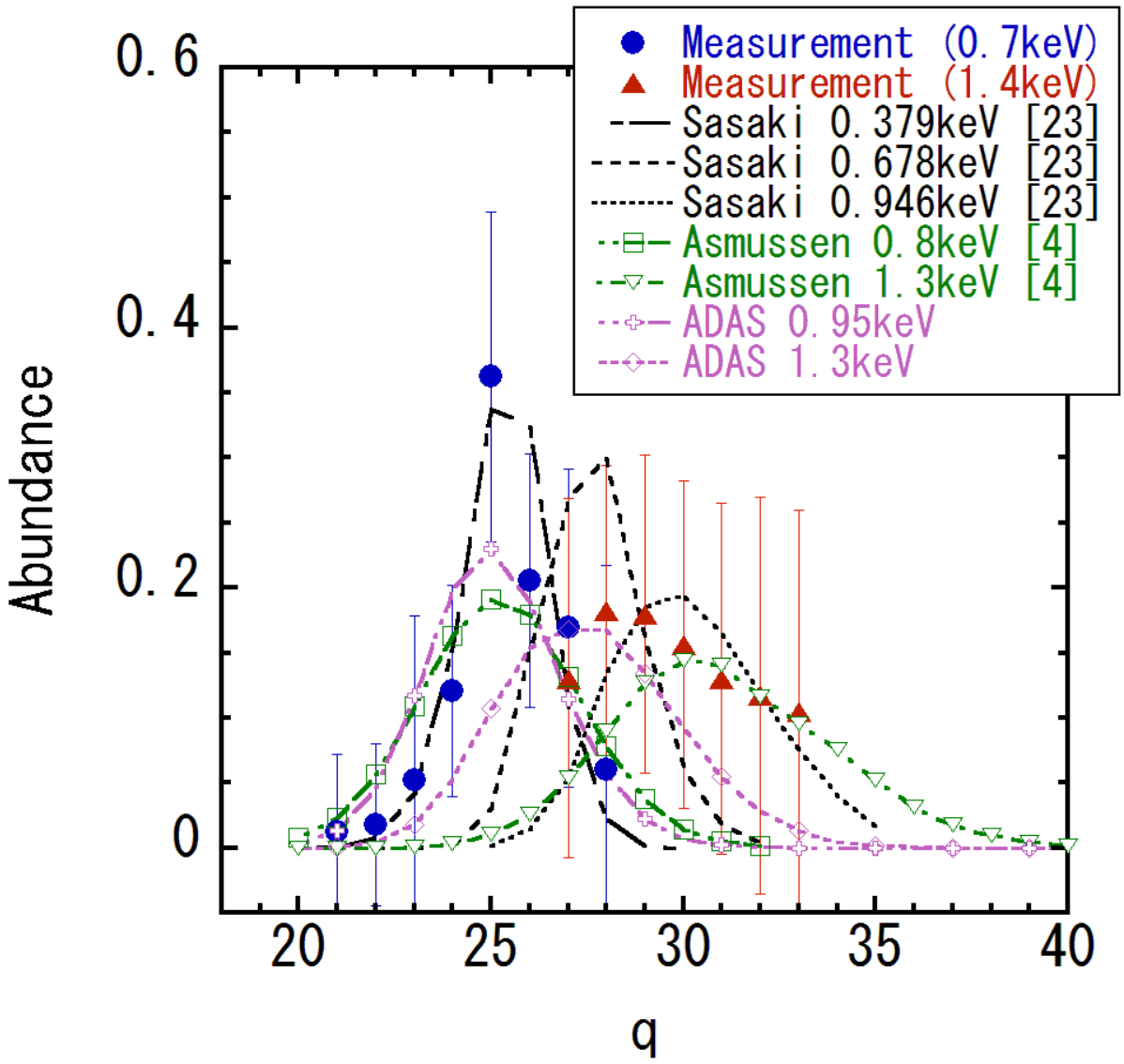

Fig. 8 Charge distribution of tungsten ions obtained by fitting to the measured LHD spectra (● and ▲), and calculated ones in ionization equilibrium obtained in [23](black lines), in [4] (green lines), and in [4] (purple lines).

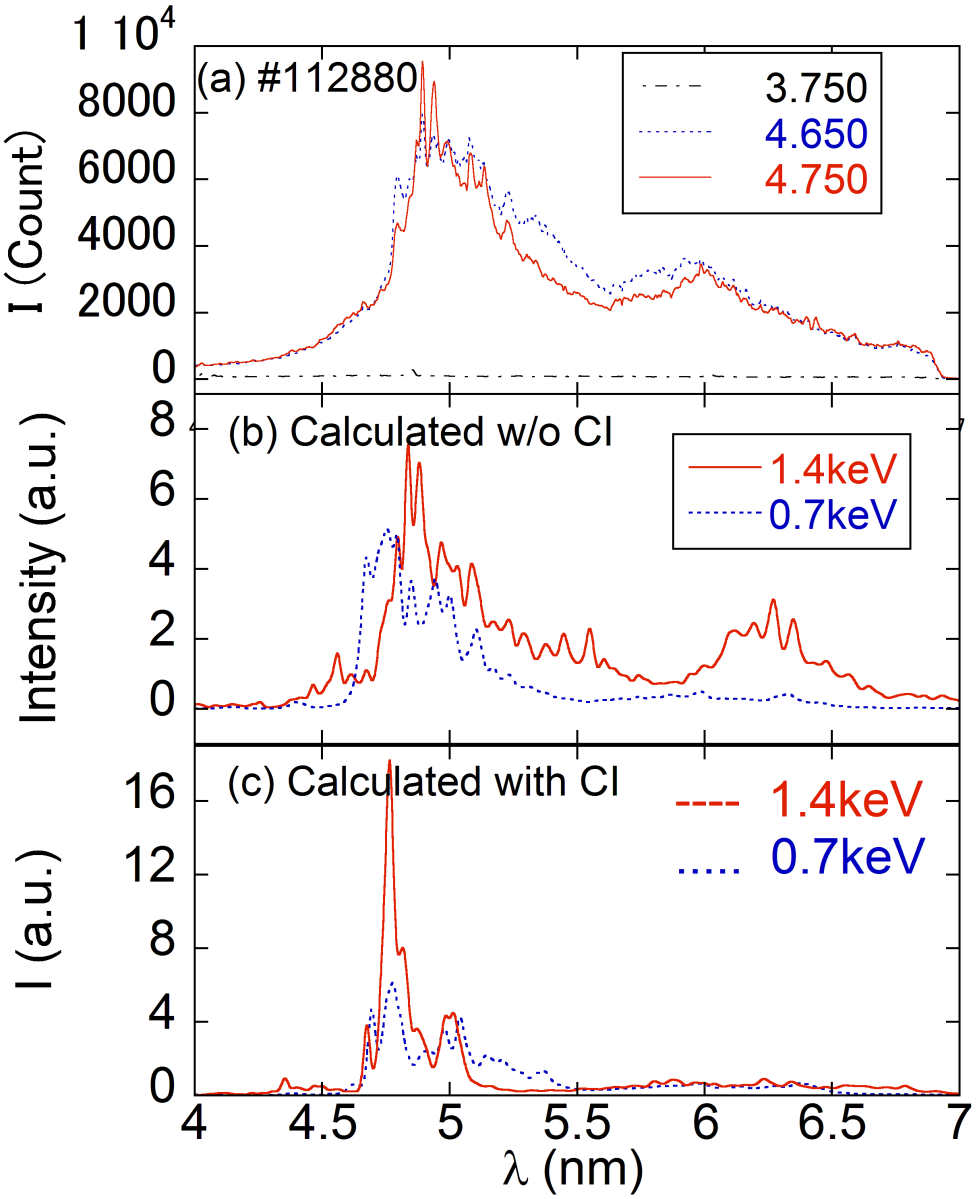

Fig. 9 (a) Tungsten EUV spectra at 3.75s (black) before pellet injection of 3.80s, at 4.65s (blue dashed line), and at 4.75s (red solid line) measured in the same LHD NBI-discharge #112880. (b) Calculated EUV spectra with atomic modeling without configuration interactions for electron temperature 0.7keV (blue dashed line) and 1.4keV (red solid line). (c) Calculated EUV spectra with atomic modeling with configuration interactions for electron temperature 0.7keV (blue dashed line) and 1.4keV (red solid line).

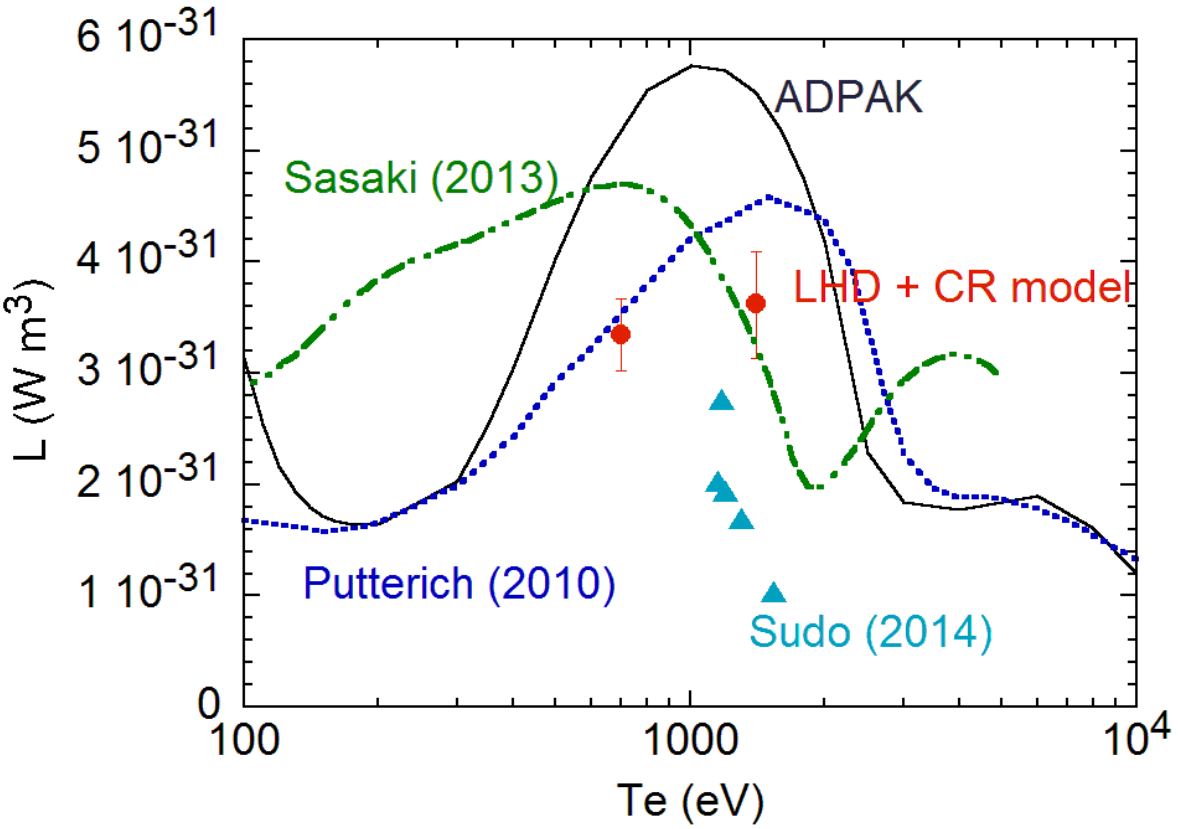

Figure 10 Radiation power rates L estimated with the ion abundance distributions obtained from the EUV spectra and CR model calculation (dots), calculated with original ADPAK [3] (solid line), by Sasaki and Murakami [23] (dot-dashed line), and by Pütterich et al [9] (dotted line), and estimated from bolometer measurements in LHD plasmas [34] (triangles).